JTTEE5 18:35–49
DOI: 10.1007/s11666-008-9279-9
1059-9630/$19.00 © ASM International

Microstructural and Tribological Investigation of High-Velocity Suspension Flame Sprayed (HVSFS) Al_2O_3 Coatings

Giovanni Bolelli, Johannes Rauch, Valeria Cannillo, Andreas Killinger, Luca Lusvarghi, and Rainer Gadow

(Submitted February 6, 2008; in revised form June 13, 2008)

Al_2O_3 coatings were manufactured by the high-velocity suspension flame spraying (HVSFS) technique using a nanopowder suspension. Their structural and microstructural characteristics, micromechanical behavior, and tribological properties were studied and compared to conventional atmospheric plasma sprayed and high-velocity oxygen-fuel-sprayed Al_2O_3 coatings manufactured using commercially available feedstock. The HVSFS process enables near full melting of the nanopowder particles, resulting in very small and well flattened lamellae (thickness range 100 nm to 1 μm), almost free of transverse microcracking, with very few unmelted inclusions. Thus, porosity is much lower and pores are smaller than in conventional coatings. Moreover, few interlamellar or intralamellar cracks exist, resulting in reduced pore interconnectivity (evaluated by electrochemical impedance spectroscopy). Such strong interlamellar cohesion favors much better dry sliding wear resistance at room temperature and at 400 °C.

Keywords HVSFS, nano Al_2O_3, suspension flame spraying, wear resistance

1. Introduction

Recently, there has been a considerable interest in thermal spray coatings manufactured from liquid feedstock (suspensions or precursor solutions) instead of conventional dry powders (Ref 1-13). Their employment can bring numerous potential advantages. In solution precursor or suspension sprayed coatings, the lamella size is micrometric or submicrometric; indeed, very fine droplets are produced either by nanoparticle suspensions injected in the gas jet of a thermal spray torch (Ref 4, 8-11) or by reaction of suitable precursor solutions inside the jet itself (Ref 1-3, 11-13). Peculiar microstructures are thus obtained, different from those of conventional thermally sprayed coatings and having improved thermomechanical behavior (for instance, better thermal cycling resistance for thermal barrier coatings) (Ref 1, 2, 13). Moreover, the very small lamella size can result in much better coating surface finish, reducing or eliminating the need for costly machining operations (near-net-shape manufacturing) (Ref 8, 9, 14). Heat-sensitive materials, which could be altered by ordinary thermal spray processes, can largely preserve their desired chemical and structural properties when deposited by these techniques. So, perovskite layers for SOFCs cathodes (Ref 5, 10) or photocatalytically active TiO_2 coatings with high anatase content (Ref 6, 7) can be manufactured. Very importantly, liquid feedstock allows larger flexibility in the choice of coating thickness: not only can thick coatings be produced for applications like thermal barrier coatings (Ref 1-3), but thinner films (thickness of about 50 μm or possibly less) having excellent quality can also be manufactured, thanks to the very small lamella size (Ref 4, 8, 15, 16). By contrast, the larger lamella size in conventional thermal spraying processes, where dry powders are employed, imposes a minimum limit in deposit thickness, because a certain number of superimposed lamellae layers is always needed to obtain a good thermally sprayed coating (Ref 17). These new processes can therefore fill the gap existing between thin film deposition technologies (PVD, CVD: thickness normally ≤10 μm (Ref 18)) and thick (≥100 μm) film techniques: until now, only wet chemical processes (electrodeposition and electroless deposition) can operate inside this thickness range (Ref 18), but they can have disadvantages like long processing time, limited flexibility in material choice, and possible safety/environmental problems, as deposition baths often contain dangerous substances.

Up to now, most attempts at liquid feedstock spraying have been performed using the plasma-spraying technique (Ref 1-7). Although its high versatility makes it a reasonable choice for liquid feedstock processing, some problems exist, especially concerning liquid feedstock injection into the plasma jet. Specifically, it is difficult to inject all (or most) of the atomized solution or suspension droplets in the plasma jet core, where proper solvent evaporation, particle melting, or precursors reaction can

Giovanni Bolelli, Valeria Cannillo, and **Luca Lusvarghi**, Department of Materials and Environmental Engineering, University of Modena and Reggio Emilia, Via Vignolese 905, I-41100 Modena (MO), Italy; and **Johannes Rauch, Andreas Killinger,** and **Rainer Gadow**, Institute for Manufacturing Technologies of Ceramic Components and Composites (IFKB), Universität Stuttgart, Allmandring 7b, D-70569 Stuttgart, Germany. Contact e-mail: giovanni.bolelli@unimore.it.

be produced. This sometimes leads to defective coatings (containing unmelted or unreacted material) (Ref 2, 3, 6, 10, 11). Very recently, the attention has also been devoted to modifying the high-velocity oxygen-fuel (HVOF) flame spraying technique in order to spray suspension feedstock, with very promising results (Ref 8, 9, 16). In the new high-velocity suspension flame spraying (HVSFS) process (Ref 8, 16), where a gas-fuelled HVOF torch has been adapted for liquid feedstock, the problem of feeding the suspension to the jet core is largely solved by the axial injection system of the torch. It has been shown that other problems may arise, like deposition of the suspension inside the combustion chamber resulting in process instabilities and defects in the coatings (Ref 19), but these troubles can be overcome, resulting in layers with excellent quality. Moreover, compared to the plasma-spraying technique, low coating defectiveness is also ensured by the very high particle velocity in the gas jet.

Research is thus ongoing to investigate the deposition of various kinds of coatings by HVSFS, including ceramics and glasses. Particularly, this paper will deal with Al_2O_3, one of the ceramic materials most commonly employed in the thermal spray industry. It has a relatively low cost, it possesses high hardness and chemical stability, making it suitable for various wear-resistant applications also in corrosive environments, and it is an excellent electrical insulator, making it a frequent choice for dielectric layers and supports for sensors, heating elements, etc… (Ref 20). Conventional thermally sprayed Al_2O_3, however, has numerous limitations: coatings are porous (therefore, not protective against corrosion of the substrate) (Ref 21, 22), rough (costly post-deposition machining is often required) (Ref 23), interlamellar cohesion is usually a very critical weak point for tribological applications (Ref 24-27), and the high thickness of the coating can, in various instances, be undesirable: for example, it is undesirable in some mechanical components, when strict dimensional and geometrical tolerances are required, or in electrical/electronic equipment, when devices to be heated must not offer excessively high thermal insulation. Thus, improvements can be expected by the use of the HVSFS spraying technique, enabling the deposition of thinner coatings with better cohesion between submicron-sized lamellae, and lower porosity with much smaller pores. This paper will therefore characterize the microstructural, micromechanical, and tribological properties of thin HVSFS-deposited Al_2O_3 layers and compare them with conventional thick atmospheric plasma sprayed (APS) and HVOF-sprayed Al_2O_3 coatings.

2. Experimental

A commercially available nanosized Al_2O_3 powder (Tai Micron, 150 nm particle size) was employed to prepare an isopropanol-based suspension (80 wt.% isopropanol, 20 wt.% Al_2O_3 powder). A SEM micrograph of this powder is shown in Fig. 1. The suspension was produced by attrition-milling with 2.5-mm diameter ZrO_2 balls.

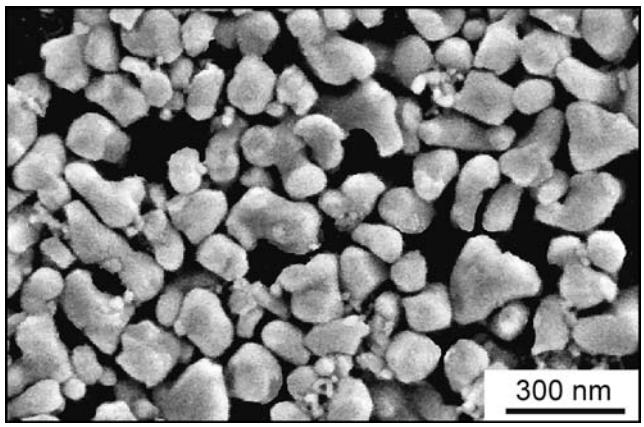

Fig. 1 SEM micrograph of the Al_2O_3 nanopowder

Table 1 HVSFS deposition parameters

Fuel (propane) flow rate, slpm	65
Oxygen flow rate, slpm	350
Suspension flow rate, mL/min	100
Spray distance, mm	100
Torch traverse speed, mm/s	1000
Pass distance, mm	2
Number of cycles	10
Cooling system	Compressed air jets

HVSFS deposition was performed using a GTV Top Gun-G torch, modified in order to inject liquid suspensions instead of dry powder feedstock. A 22-mm-long combustion chamber, with a 135-mm-long expansion nozzle, was employed. A special feeding system (whose details are confidential), providing a constant flow of suspension, was used to feed the suspension to the torch. Deposition parameters are listed in Table 1. The substrates were $(50 \times 50 \times 3)$ mm^3 titanium plates, degreased using isopropanol and grit-blasted using 200 μm alumina grits at 5 bar pressure immediately before spraying.

For comparative purposes, conventional APS and HVOF-sprayed Al_2O_3 coatings were also manufactured. The APS coatings were deposited using a GTV F6 plasma torch. The HVOF coatings were deposited using a GTV Top Gun-G gas-fuelled torch, i.e. the same torch which was employed in the HVSFS process. In this case, the torch was employed in its standard configuration, with no modifications to the injection system. The differences between the presently considered HVOF and HVSFS coatings, therefore, are independent of the torch architecture and are determined solely by the nature of the feedstock, and by the different spray parameters which are imposed by the nature of the feedstock itself. The comparison between these coatings can therefore return useful indications on the advantages granted by the use of suspensions.

Deposition parameters are indicated in Table 2. These are standard deposition parameters which are routinely employed for the deposition of Al_2O_3 coatings, using the above-mentioned torches.

Table 2 APS and HVOF deposition parameters

APS deposition parameters		HVOF deposition parameters	
Ar/H_2 flow rate, slpm	44/10	Combustion chamber type	22/8/200
Current, A	700	Fuel (acetylene) flow rate, slpm	70
Nozzle diameter, mm	6	Oxygen flow rate, slpm	140
Spray distance, mm	100	Spray distance, mm	200
Torch traverse speed, mm/s	400	Torch traverse speed, mm/s	400
Pass distance, mm	3	Pass distance, mm	2
Number of cycles	2	Number of cycles	9
Cooling system	Compressed air jets	Cooling system	Compressed air jets
Powder	40.05.0 (GTV) −25 + 5 μm	Powder	40.05.0 (GTV) −25 + 5 μm
Feeder disk rotation speed, rpm	4	Feeder disk rotation speed, rpm	1.5
Carrier gas (Ar) flow rate, slpm	7	Carrier gas (N_2) flow rate, slpm	25

Phase composition was assessed by X-ray diffraction (XRD, X'Pert Pro, PANAlytical, Almelo, The Netherlands). The ratio between α-Al_2O_3 and γ-Al_2O_3 was determined by the intensities of the (311) and (400) peak, respectively, according to the formula (1), already employed in Ref 28:

$$R_{\alpha/\gamma} = \frac{1}{1 + 1.08\frac{I_{(400)}}{I_{(311)}}} \quad \text{(Eq 1)}$$

where $I_{(311)}$ is the integral intensity of the α-Al_2O_3 (311) peak; $I_{(400)}$ the integral intensity of the γ-Al_2O_3 (400) peak; and 1.08 the correction coefficient, accounting for structure factors, peak multiplicities, and unit cell volumes.

Polished cross sections (cold-mounted in resin, ground and eventually polished with 0.5 μm diamond slurry) and fractured sections (obtained by breaking thin bar samples in liquid nitrogen) were observed by scanning electron microscope (SEM, XL-30, FEI, Eindhoven, The Netherlands). Porosity was measured by image analysis (NIH ImageJ v1.34) on polished sections, using 1000× SEM micrographs, as described in Ref 29. Specifically, percentage porosity, pore roundness, average pore area, and percentage of transverse cracks (defined as the percentage of pores having major axis angle between 45 and 135° among pores with circularity <0.5) were computed. Coating thickness was also measured by image analysis. The surface roughness was measured by optical confocal profilometry (Conscan profilometer, CSM Instruments, Peseux, Switzerland).

In order to obtain a more comprehensive characterization of the coatings' porosity, overcoming the limitations of the image analysis technique in accounting for the smaller defects and in determining the pore interconnectivity degree (a key factor in assessing coating cohesion and protectiveness), the electrochemical impedance spectroscopy (EIS) technique was also employed. As thoroughly described in Ref 30, 31, fitting the electrochemical impedance spectra of the coatings with a suitable equivalent circuit returns quantitative data (resistance and capacitance values) related to coating porosity, pore interconnectivity, pore size and morphology. Tests were performed with a PC-controlled Ametek VersaStat3 potentiostatic/galvanostatic instrument (Princeton Applied Research, UK), using a 3-electrode cell (EG&G K0235 flat cell) where the sample is the working electrode (1 cm^2 exposed surface), a Pt grid is the counter-electrode, and the reference electrode is an $Ag/AgCl/KCl_{(sat.)}$ electrode. The electrolyte was a 0.01 M $K_3Fe(CN)_6/K_4Fe(CN)_6$ aqueous solution, chosen for its stability and high redox reversibility, as also described in Ref 31. Tests were performed at room temperature, in equilibrium with the environment; the voltage perturbation amplitude was 10 mV (versus open circuit potential), the scanned frequency range was 100 kHz to 1 mHz (8 points/decade). Tests were started with a 30-min delay to allow full impregnation of the coating by the test solution and complete stabilization of the open circuit potential. Results were fitted using the Frequency Response Analyser software (Eco Chemie B.V., Utrecht, The Netherlands).

Depth-sensing Berkovich nanoindentation (Nanoindenter, CSM Instruments) was performed at loads of 100 mN (loading/unloading rate 80 mN/min, holding time 10 s), 300 mN (loading/unloading rate 240 mN/min, holding time 10 s), 500 mN (loading/unloading rate 400 mN/min, holding time 10 s), in order to probe increasingly large material volumes. Hardness and elastic modulus were computed (Oliver-Pharr procedure (Ref 32), Poisson's ratio assumed to be 0.23).

Rotating unidirectional ball-on-disk tests were performed with a pin-on-disk tribometer (CSM Instruments), using a spherical pin (6 mm diameter) consisting of sintered Al_2O_3 (manufacturer's nominal hardness 19 GPa) sliding against a flat coated sample, fixed on a rotating disk. Test parameters included 500 m sliding distance, 0.20 m/s relative sliding speed, 5 N normal load. Tests were performed at room temperature (25 °C, 60% relative humidity) and at 400 °C. The friction coefficient was on-line monitored during the test; the sample wear rate was assessed by optical confocal profilometry (Conscan profilometer, CSM Instruments). Worn samples and wear debris were also observed by SEM (XL30 and Environmental SEM XL40, FEI) at the end of the test.

All coatings were tested both in as-deposited condition and after manual polishing to $R_a \approx 0.5$ μm (thickness reduction after polishing was about 10 μm, measured by non-destructive eddy-current system: C-Gage, Sonatest, Old Wolverton, UK).

3. Results and Discussion

3.1 Microstructure and Porosity

All coatings consist mainly in γ-Al_2O_3, together with some glassy phase, recognizable from the amorphous hump at $35° < 2\theta < 40°$ in XRD patterns (Fig. 2); these metastable phases are produced by rapid lamella solidification from the melt upon impact, as largely documented in literature (Ref 33, 34). Minor amounts of α-Al_2O_3 exist, which mostly reflect the embedment of unmelted material or in-flight resolidified material: consistently with a previous research (Ref 28), the overall amount of unmelted material is larger in the HVOF coating than in the APS one (Table 3), due to the lower gas temperature in HVOF torches (Ref 35). Very remarkably, the HVSFS coating contains even less α-Al_2O_3 than the APS one (Table 3), indicating that the process conditions enabled near full melting of the powder, which is a key factor to achieve high density and cohesion in thermally sprayed ceramics. In the above-mentioned previous research, it was shown that even conventional HVOF spraying of agglomerated nanostructured powders could not achieve such condition (Ref 28).

The HVOF coating possesses lower porosity (from image analysis, Table 4) than the APS one, because, although it contains more numerous inclusions of unmelted or in-flight resolidified particles, revealed by XRD and clearly noticeable in SEM micrographs as well (compare Fig. 3a to Fig. 3c; circles indicate some of the recognizable rounded inclusions), the very high impact velocity of the fully molten droplets enables them to flow extensively, thus adapting themselves to complex geometries, like those produced by rounded inclusions, leaving few voids, as the conclusions in Ref 28 already stated. The efficient particle flow upon impact also results in less longitudinal interlamellar defects. Moreover, a lower amount of intralamellar transverse microcracking is also found (compare Fig. 3b to Fig. 3d; some longitudinal and transverse cracks in the APS coating are indicated by arrows). The lower degree of transverse microcracking was also noted on HVOF-sprayed alumina single splats (Ref 36) and was attributed to different lamella solidification histories (Ref 28, 36).

Lamellae morphologies are also significantly different, the APS ones being thicker and having larger and more clearly recognizable columnar grains: the lower velocity and higher average temperature of APS particles than HVOF ones upon impact (Ref 35) cause lower flattening degree and very different solidification histories (Fig. 4a, b). On the fracture surface of the HVOF coating, some of the numerous rounded inclusions are also visible (Fig. 4b). Less interlamellar defects and less intralamellar cracks in HVOF Al_2O_3 are quantitatively reflected by higher overall pore roundness and lower amount of vertical cracks (Table 4).

The microstructure of the HVSFS coating is remarkably different from the former ones (Fig. 3e, f). In particular, porosity is much lower and pores seem very small and rounded (Fig. 3e, f, Table 4). On the one hand, better particle melting (as noted above) favors very high interlamellar cohesion. On the other hand, lamellae are significantly smaller and thinner (Fig. 4c), so that pores due to imperfect interlamellar overlapping or to inclusions of unmelted or in-flight resolidified material are also much smaller. Specifically, observation of the fracture surface (Fig. 4c) indicates that the thickness of HVSFS-deposited lamellae ranges from ≤100 nm to ~1 μm, whereas HVOF- and APS-deposited ones (Fig. 4a, b) are generally thicker than 1 μm. Accordingly, on the surface of the HVSFS-deposited coatings, lamellae having diameters ranging from about 100 nm to few micrometers are recognizable (Fig. 5). By contrast, in conventional APS and HVOF coatings, lamellae normally have a diameter of several tens of micrometers.

Although the lamellae in the HVSFS coating are smaller than in the APS and HVOF ones, many of them are somewhat larger than the Al_2O_3 particles contained in

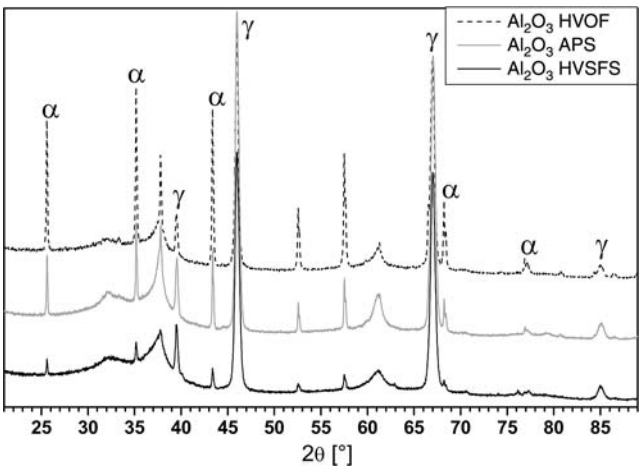

Fig. 2 X-ray diffraction patterns of APS, HVOF, and HVSFS Al_2O_3 coatings

Table 3 α-Al_2O_3/γ-Al_2O_3 ratio from Eq 1

Coating	α-Al_2O_3/γ-Al_2O_3, %
APS Al_2O_3	7.5
HVOF Al_2O_3	22.8
HVSFS Al_2O_3	2.8

Table 4 Image analysis results and roughness measurement

	APS Al_2O_3	HVOF Al_2O_3	HVSFS Al_2O_3
Porosity, %	11.0 ± 1.1	8.6 ± 0.5	4.4 ± 2.3
Average pore size, μm^2	1.58 ± 0.11	1.71 ± 0.06	0.71 ± 0.08
Pore roundness	0.64 ± 0.02	0.67 ± 0.01	0.74 ± 0.01
% Vertical cracks	33.6 ± 6.3	18.5 ± 6.5	15.8 ± 6.9
Thickness, μm	114 ± 5	113 ± 5	65 ± 4
R_a, μm	4.29 ± 0.63	3.38 ± 0.51	4.86 ± 0.46

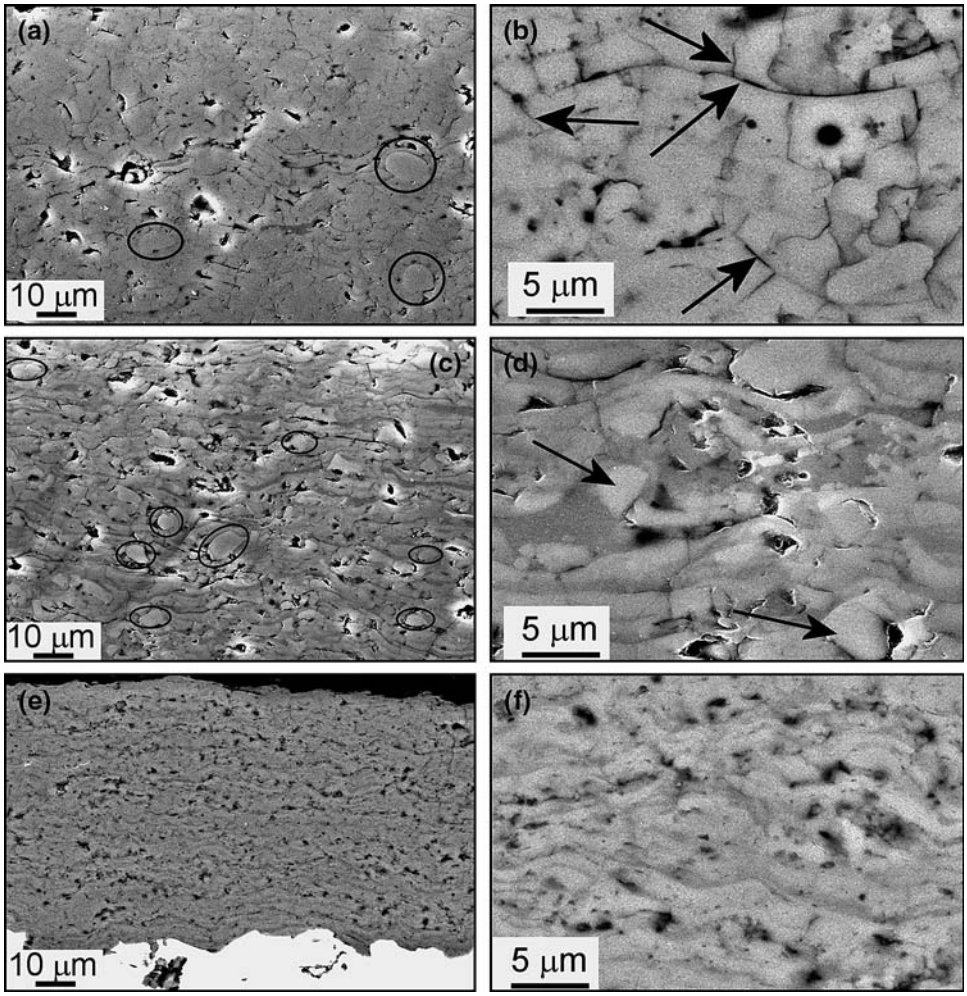

Fig. 3 SEM micrographs of polished cross sections: (a, b) APS Al_2O_3 (circles: rounded unmelted inclusions; arrows: longitudinal and transverse cracks); (c, d) HVOF Al_2O_3 (circles and arrows: rounded unmelted inclusions); and (e, f) HVSFS Al_2O_3

the suspension (Fig. 1), having a diameter of about 150 nm. Recent studies have indeed shown that, in suspension-sprayed coatings, the lamella size mostly depends on the formation of nanoparticle agglomerates, rather than on the individual nanoparticle size (Ref 11, 37-41). The following steps have accordingly been proposed in the pertinent literature. When drops of a liquid feedstock (nanoparticle suspensions or solution precursors) are injected in a thermal spray jet (plasma or HVOF), they undergo an aerodynamic break-up into small-size droplets. Subsequently, the nanoparticles contained in a droplet form an agglomerate as the liquid phase evaporates. These agglomerates can be further subdivided into smaller-sized ones (Ref 11, 40, 41). Melting of these agglomerates and impact of the resulting molten droplets onto the substrate produces the lamellae.

Agglomerates are probably being formed during the present HVSFS deposition of the Al_2O_3 nanoparticle suspension, as many lamellae are generally larger than the initial nanoparticles. Only few lamellae in Fig. 5 have a size comparable to that of the primary particles (Fig. 1). Judging from the micrographs in Fig. 4(c) and Fig. 5, however, it can be inferred that most of these agglomerates are probably not larger than 1 μm. Accordingly, numerical studies have shown that the strong turbulence inside the combustion chamber of an HVOF torch makes the aerodynamic break-up of the liquid drops particularly severe (Ref 37), resulting in micron-sized droplets, smaller than those obtained by radial injection of the liquid feedstock in a plasma jet (Ref 37, 38). These very small droplets probably produce consistently small (micron- or submicron-sized) agglomerates. Moreover, the strong turbulence of the HVOF gas jet may favor further break-up of the agglomerates. Possibly, some agglomerates are completely disintegrated, thus resulting in the appearance of some lamellae having a size analogous to the primary particles.

Consequently, lamellae are definitely smaller than those obtained by the deposition of conventional dry powders, notwithstanding the agglomeration phenomena.

As shown by the fracture surface (Fig. 4c), the solidification of such small lamellae results in smaller columnar

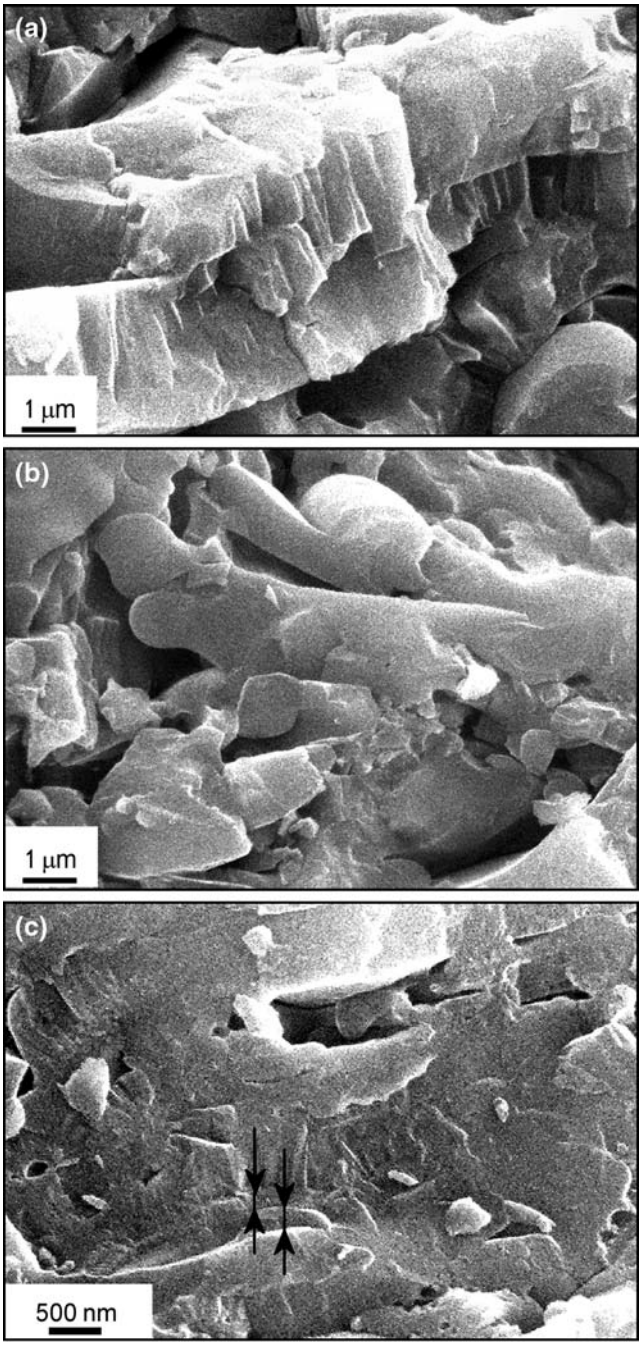

Fig. 4 Fracture surfaces of APS (a), HVOF (b), and HVSFS (c) Al_2O_3 coatings (arrows indicate two thin lamellae)

grains (≤100 nm wide) than in conventional APS and HVOF-deposited coatings.

Despite the smaller size of the lamellae, the roughness of the HVSFS coating is quite high (Table 4); indeed, ''bump-like'' features are scattered throughout its surface (Fig. 6). The occurrence of similar features has already been documented in previous literature reports (Ref 10, 19, 41), and two explanations are possible. The first one has been proposed in Ref 41, where Oberste Berghaus et al.

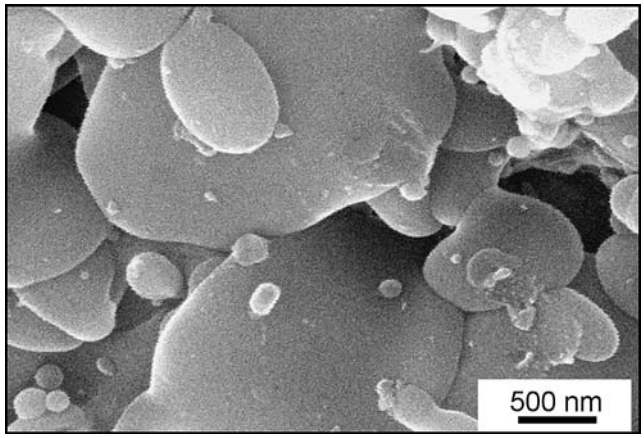

Fig. 5 HVSFS Al_2O_3 coating surface: high-magnification detail showing some lamellae

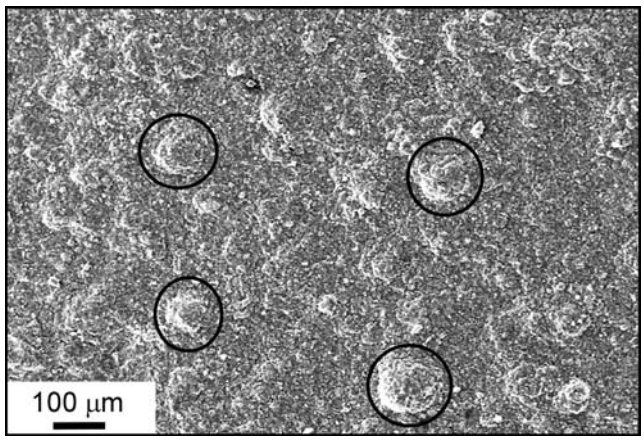

Fig. 6 HVSFS Al_2O_3 coating surface: general view. Circles indicate some ''bump-like'' features

suggested that the smaller particles (resulting from extensive disintegration of an agglomerate), because of their very low inertia, follow the radially deflecting gas flow in the stagnation point above the substrate and travel laterally along the substrate surface. They probably attach onto the most prominent roughness asperities, creating the growing ''bumps''. Alternatively, the surface ''bumps'' can be caused by the formation of solid deposits on the walls of the torch's combustion chamber and barrel during spraying: such deposits were indeed noted inside the torch by visual inspection at the end of the deposition process. From time to time, large portions of material can be detached from these deposits and be projected toward the substrate, thus giving rise to the large ''bumps'' in Fig. 6. In a previous paper on HVSFS-deposited glass coatings (Ref 19), the authors have already reported the appearance of large surface ''bumps'' as a consequence of the formation of solid deposits inside the torch. The formation of such deposits is due to turbulence effects inside the combustion chamber: ongoing research (which will be the subject of future

papers) has very recently indicated that deposits can be prevented by modifying the combustion chamber's geometry, and, accordingly, the ''bumps'' are largely suppressed. This suggests that deposits are actually the main reason for the appearance of ''bumps'' in the present HVSFS coatings.

It is extremely important to note the lack of intralamellar cracking in small HVSFS lamellae (Fig. 5): the small lamella size probably limits the quenching stresses, so that microcracking during cooling is reduced or suppressed.

Also, the HVSFS coating is thinner than the APS and HVOF ones (Table 4), as expected. It is therefore confirmed that HVSFS has the unique capability of providing low thickness coatings with extremely low defectiveness. As discussed previously, the conventional APS and HVOF coatings have thicker lamellae than the HVSFS one: reducing the thickness of a conventional coating into the ~50 μm range would therefore result in high inhomogeneity and defectiveness, because lamellae would be too coarse compared to the low coating's thickness, as also stated in Ref 16. By contrast, the thin HVSFS lamellae result in homogeneous, dense thin coatings.

EIS results corroborate SEM observations and image analysis results. EIS spectra shown in Fig. 7(a) were fitted with the equivalent circuit formerly proposed by Zhang and Desai (Ref 31) for plasma-sprayed Y-PSZ thermal barrier coatings (Fig. 7b). Their interpretation of the physical meaning of the electrical elements was adopted in this study. The equivalent circuit consists of the following elements: R_S is the cell resistance; R_C, C_C the coating resistance and capacitance; R_P, C_P the pore resistance and capacitance; and R_T, C_D the resistance and capacitance of the electrolyte/working electrode interface reaction.

Specifically, the coating resistance R_C depends on the coating thickness and on the overall coating resistivity ρ_C, according to the relation:

$$R_C = \rho_C \frac{t_C}{A} \qquad \text{(Eq 2)}$$

where A is the exposed area (= 1 cm^2 in this case) and t_C the coating thickness.

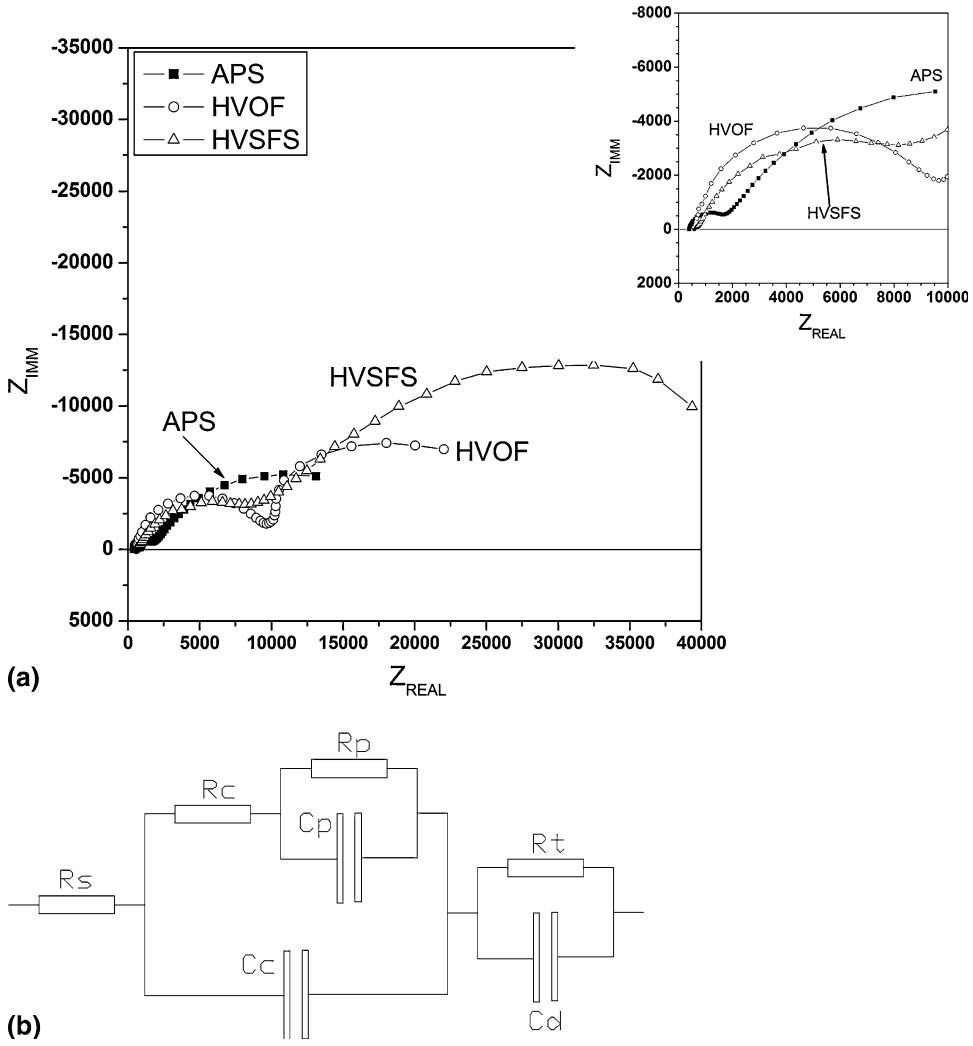

Fig. 7 EIS test results (a, Nyquist plot) and equivalent circuit used for spectra fitting (b)

Table 5 EIS test results

	APS Al_2O_3	HVOF Al_2O_3	HVSFS Al_2O_3
R_S, Ω	426 ± 6	632 ± 13	841 ± 42
ρ_C, 10^3 Ω * cm	124.7 ± 9.2	466.9 ± 53.0	956.9 ± 32.0
$(C_C * t_C)/A$, μF/m	53.5 ± 1.9	45.5 ± 4.6	8.3 ± 2.6
R_P, Ω	2417 ± 182	2222 ± 584	10340 ± 1075
C_P, μF	3087 ± 259	3652 ± 366	722 ± 92
R_T, Ω	11265 ± 728	15490 ± 403	36250 ± 5869
C_D, μF	8500 ± 28	2658 ± 96	2648 ± 595

Charge transfer can take place both through the bulk ceramic and through the electrolyte filling up the pores; the latter contribution is particularly important, since the resistance of the bulk ceramic material is extremely high (several order of magnitudes larger than experimentally observed resistivities). Thus, it has been suggested that a linear relationship exists between coating resistivity and its porosity. Analogously, the coating capacitance C_C depends both on the ceramic capacitance and on the pore capacitance, so that the following relation has been proposed:

$$C_C \frac{t_C}{A} \approx \varepsilon_0 \varepsilon_1 + \varepsilon_0 (\varepsilon_2 - \varepsilon_1) \frac{K}{t_{DL}} P \qquad \text{(Eq 3)}$$

where ε_0 is the vacuum dielectric constant; ε_1 the ceramic material dielectric constant; ε_2 the electrolyte dielectric constant; K the correction factor; t_{DL} the thickness of the electric double layer around pore surfaces; and P the porosity.

It can be noted that the HVSFS coating has the highest resistivity and lowest capacitance (Table 5). Moreover, the trends of ρ_C and $C_C * t_C/A$ versus coating's porosity (as determined by image analysis) can actually be fitted with linear relations, obtaining satisfactory correlations (Fig. 8a): this indicates the validity and applicability of the above equations.

These results confirm the much lower defectiveness of the HVSFS coating, corroborating the image analysis results, and show that such low defectiveness is correlated to higher coating protectiveness toward the substrate, since the HVSFS-coated system opposes higher impedance against electrochemical charge transfer phenomena.

The electrode interface resistance R_T is also extremely useful to characterize pore interconnectivity. This is probably the most important result returned by the EIS technique; indeed, pore interconnectivity cannot be computed nor estimated by image analysis. The good correlation between porosity, R_C and C_C proves that the EIS results are meaningful and testifies to the reliability of the pore interconnectivity analysis.

According to Ref 30, R_T can be expressed as:

$$R_T = \rho_E \frac{t_{DL}}{A_E} \qquad \text{(Eq 4)}$$

where ρ_E is the electrolyte resistivity; A_E the exposed electrode area; and t_{DL} the thickness of the electric double layer on the electrode surface. The exposed electrode area A_E corresponds to the substrate surface area which the electrolyte can reach through interconnected porosity; therefore, A_E is directly related to the amount of interconnected porosity. R_T in the HVSFS-coated system is more than 3 times higher than in the APS coated system and more than 2 times higher than in the HVOF-coated one (Table 5); thus, interconnected porosity in the HVSFS coating is much lower than in the conventional APS and HVSFS ones, notwithstanding its lower thickness. If we assume that the interconnected pore volume can be approximately estimated as $V \approx A_E * t_C$ (i.e., the exposed substrate area multiplied by the coating thickness), then the following relation can be employed to evaluate the ratio between the volumes of interconnected pores in different coatings:

$$\frac{V_2}{V_1} \approx \frac{A_{E2}}{A_{E1}} \frac{t_2}{t_1} = \frac{R_{T1}}{R_{T2}} \frac{t_2}{t_1} \qquad \text{(Eq 5)}$$

where $V_{1,2}$ is the interconnected pore volume of coatings 1 and 2; $t_{1,2}$ the thickness of coatings 1 and 2; $A_{E1,2}$ the exposed substrate area under coatings 1 and 2; and

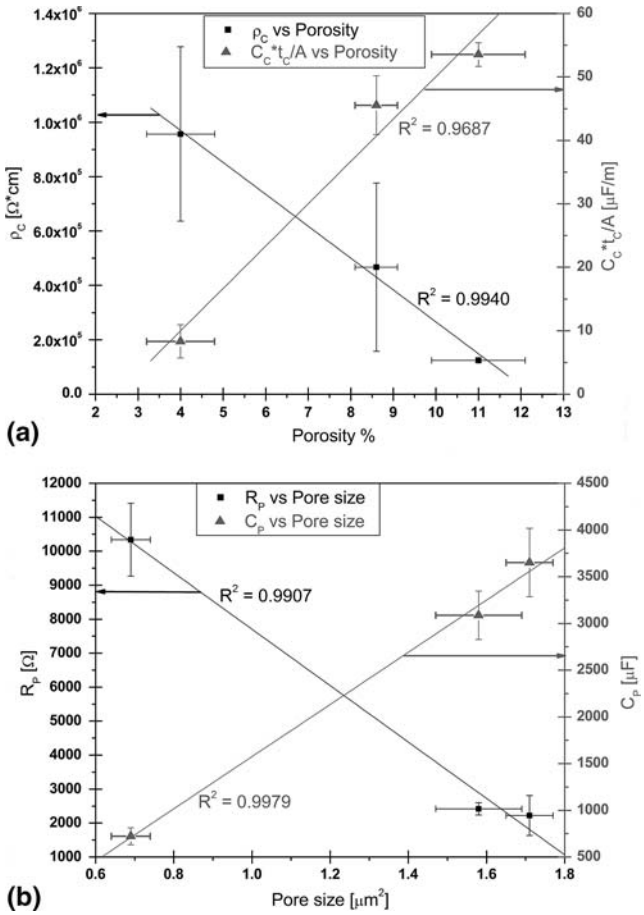

Fig. 8 Correlation between EIS fitting results and pore characteristics (from image analysis): (a) coating porosity versus resistivity (ρ_C) and normalized capacitance ($C_C * t_C/A$); (b) average pore size versus pore resistance (R_P) and capacitance (C_P)

$R_{T1,2}$ the electrode interface resistances of coated systems 1 and 2.

By employing this approximate relation using data in Table 5 (R_T) and Table 4 (coating thickness), the interconnected pore volume of the HVSFS coating is estimated to be $(24 \pm 7)\%$ of that of the HVOF coating and $(17 \pm 6)\%$ of that of APS coating. This finding confirms that the formerly noted lack of interlamellar and intralamellar cracks actually results in much lower pore interconnectivity and better protectiveness of the coating toward the substrate.

Finally, the R_P and C_P parameters can return important indications on the protectiveness provided by the different pore architectures of the various coatings. These parameters are indeed thought to describe the intrinsic electrical characteristics of pores, dependent on their size and morphology (Ref 31). Although it is not possible to obtain explicit information on the pore size and shape from R_P and C_P, the higher R_P and lower C_P exhibited by the HVSFS coating indicate that its pores, thanks to their size and shape, are capable of providing an excellent hindrance to electrical conduction phenomena across the electrolyte, thus limiting the possibility of electrochemical corrosion of the substrate. This result corroborates, once more, the previous observations on the better protectiveness of the HVSFS coating.

Moreover, the linear correlations existing between these R_P, C_P and pore size (Fig. 8b) prove, once again, the usefulness of EIS results for the microstructural characterization of thermally sprayed ceramic coatings.

3.2 Nanoindentation

The hardness of all coatings decreases as the indentation load increases (Fig. 9a), consistently with a previous study, which reported a marked indentation size effect in thermally sprayed ceramics (Ref 42). However, such decreasing behavior is significantly different between conventional coatings (APS, HVOF) and the HVSFS one. The reason of this difference lies in the fact that the lowest indentation load (100 mN) probes a very small material volume (Fig. 10a, see circle), comprising only one or few lamellae (Ref 43), whereas the greater indentation loads probe an increasingly large number of lamellae. In defective coatings (like the conventional APS and HVOF ones), the occurrence of interlamellar cracking phenomena increases as the number of probed lamellae grows. Consequently, material failure at 500 mN load is clearly noticeable in APS and HVOF coatings (Fig. 10b, cracks in and around the indentation mark are highlighted by arrows). Contrarily, in the HVSFS coating, the decrease in hardness is less marked, especially between 300 and 500 mN loads: as the HVSFS coating possesses higher cohesion strength, less cracking phenomena occur even when many lamellae are being indented. Crack formation therefore has a lower incidence on the measured hardness value, which always preserves a larger dependence on intrinsic material hardness (300 mN, 500 mN).

Accordingly, similar indentation size effects were already noted for thermally sprayed ceramics (Ref 28),

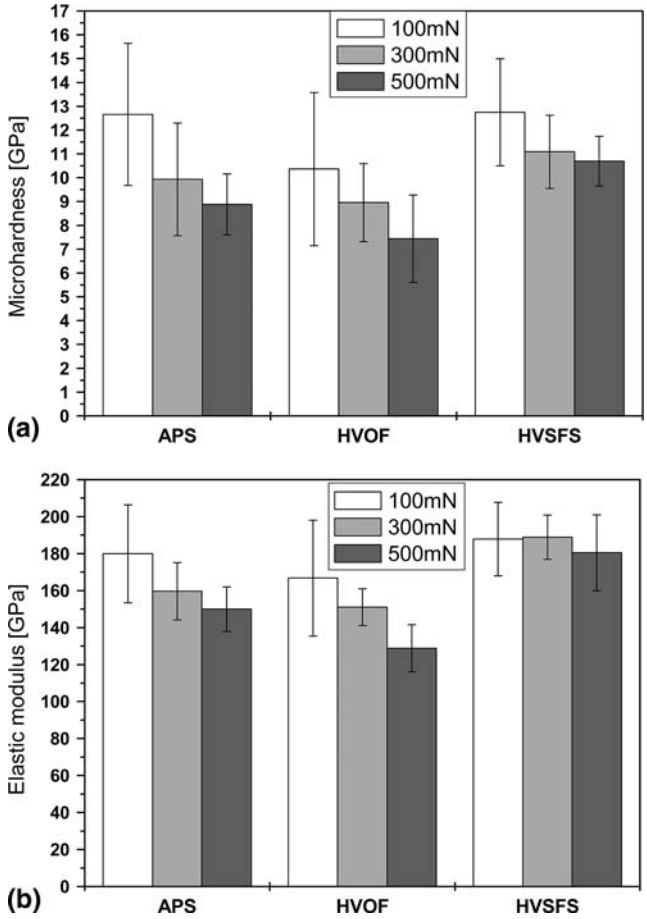

Fig. 9 Hardness (a) and elastic modulus (b) measured by depth-sensing Berkovich nanoindentation on all coatings at three different indentation loads

and the remarkable effect of cracking phenomena on the decrease in measured hardness was highlighted by a previous research (Ref 44).

A similar trend is also observed for the elastic modulus values (Fig. 9b). Indeed, as demonstrated in the above-mentioned study (Ref 44), cracking phenomena in the coating can largely decrease the elastic modulus values measured by depth-sensing indentation: the displacement of crack and pore surfaces adds a contribution to the load-displacement curve measured during indentation, and results in lower apparent modulus value (Ref 45).

These tests confirm that the much lower defectiveness and lower porosity of the HVSFS coating actually result in better interlamellar cohesion and higher resistance to cracking.

Finally, some minor remarks should also be introduced. First of all, although these size effects and their interpretation are definitely consistent with a previous study on the mechanical properties of thermally sprayed ceramic coatings (Ref 28), higher loads were adopted in that study, in order to produce relevant cracking (≥1 N) using a Vickers indenter. This difference can be due to the dissimilarity between the cracking phenomena induced by

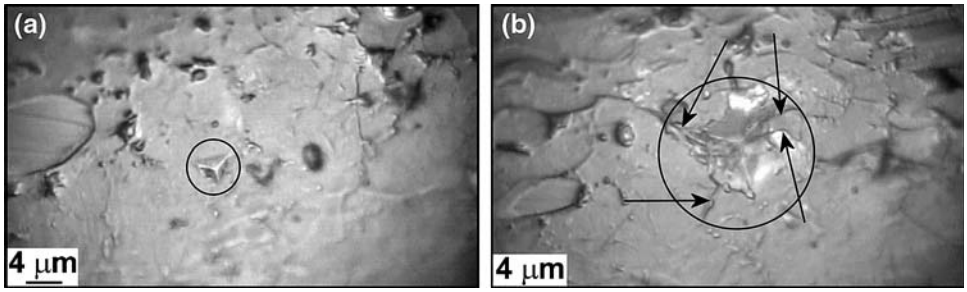

Fig. 10 Optical micrographs of 100 mN (a, see circle) and 500 mN (b, see circle) Berkovich nanoindentations on APS Al_2O_3 coating (arrows in panel b indicate indentation-induced cracks)

Berkovich and Vickers indenters, as shown by a previous paper (Ref 44): specifically, the former had been found to produce larger cracking. These considerations can also explain the differences in applied loads between the present study and the cited reference (Ref 28).

Secondly, the standard deviation of hardness values is rather large, particularly at 100 mN: due to the very small size of the indented volume, some scatter in experimental hardness values can be expected if the indentation is performed, for instance, close to a defect or on an unmelted α-Al_2O_3 particle.

Third, the HVOF coating displays lower hardness and elastic modulus than the APS one under all indentation loads, despite its porosity being lower. This could be due to the presence of a relevant amount of unmelted particles. Although the high velocity of the impinging molten droplets enables them to spread around unmelted inclusions leaving few open voids (as stated in Section 3.1), the bonding to unmelted particles is clearly less strong than the bonding between two well-molten lamellae. This can decrease hardness and modulus.

It should be noted that this result is somewhat in disagreement with the findings from a previous research comparing HVOF and APS Al_2O_3 coatings, where the HVOF coating was produced using a torch different from the present one. In that case, the HVOF coating contained a lower amount of unmelted material and exhibited higher hardness and modulus (Ref 28). So, it might be possible that, by varying the deposition conditions, a HVOF Al_2O_3 coating having somewhat better mechanical properties and wear resistance than the one presently considered could be produced.

3.3 Tribological Tests

There is a very remarkable difference between the dry sliding wear behavior of conventional APS and HVOF coatings and that of HVSFS coatings.

Indeed, conventional coatings, both as-sprayed and polished, undergo rather severe wear loss both at room temperature and at 400 °C under the present test conditions. Quite interestingly, the wear rates of APS and HVOF coatings are slightly higher at room temperature than at high temperature, and do not change much after polishing (Fig. 11), consistently with previous room

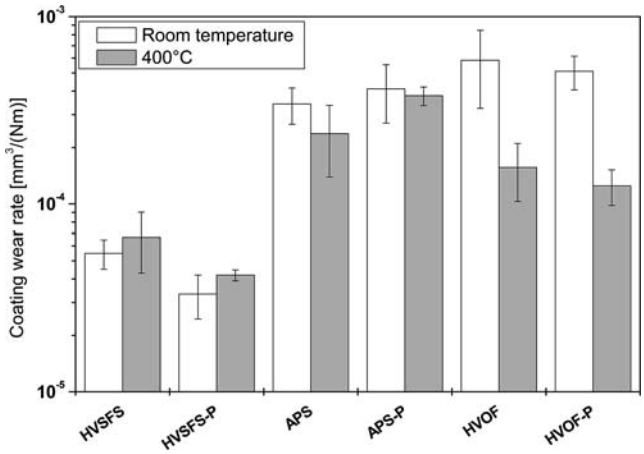

Fig. 11 Wear rates of HVSFS, APS, and HVOF coatings after ball-on-disk tests. P = polished coating

temperature ball-on-disk tests performed under similar conditions (Ref 27).

SEM micrographs confirm that a significant amount of material was removed from the APS and HVOF coatings (Fig. 12a); moreover, a layer of very fine, plastically deformed debris sticks to their wear track (Fig. 12b, c). Loose debris particles are also present on the sample surfaces at the end of the test: they consist in very fine particles forming agglomerated clusters (Fig. 12d). Sometimes, these agglomerates have a platelet-like shape (Fig. 12e). It is therefore likely that wear is occurring by brittle fracture, both on the APS or HVOF coating and on the counterpart: the detached fragments are progressively broken up while the test continues, until their small size allows them to agglomerate and stick to the wear track itself. This leads to the formation of a tribofilm, which, however, has poor adhesion to the coating surface, so that it can be easily removed (originating loose clusters of agglomerated particles, which sometimes possess lamellar shape), allowing the wear process to continue. This mechanism has already been described for thermally sprayed alumina-base coatings (Ref 27).

The HVSFS coatings, instead, undergo very moderate wear loss. On as-sprayed HVSFS coatings, no groove is found in the wear track, unlike conventional coatings (Fig. 13a).

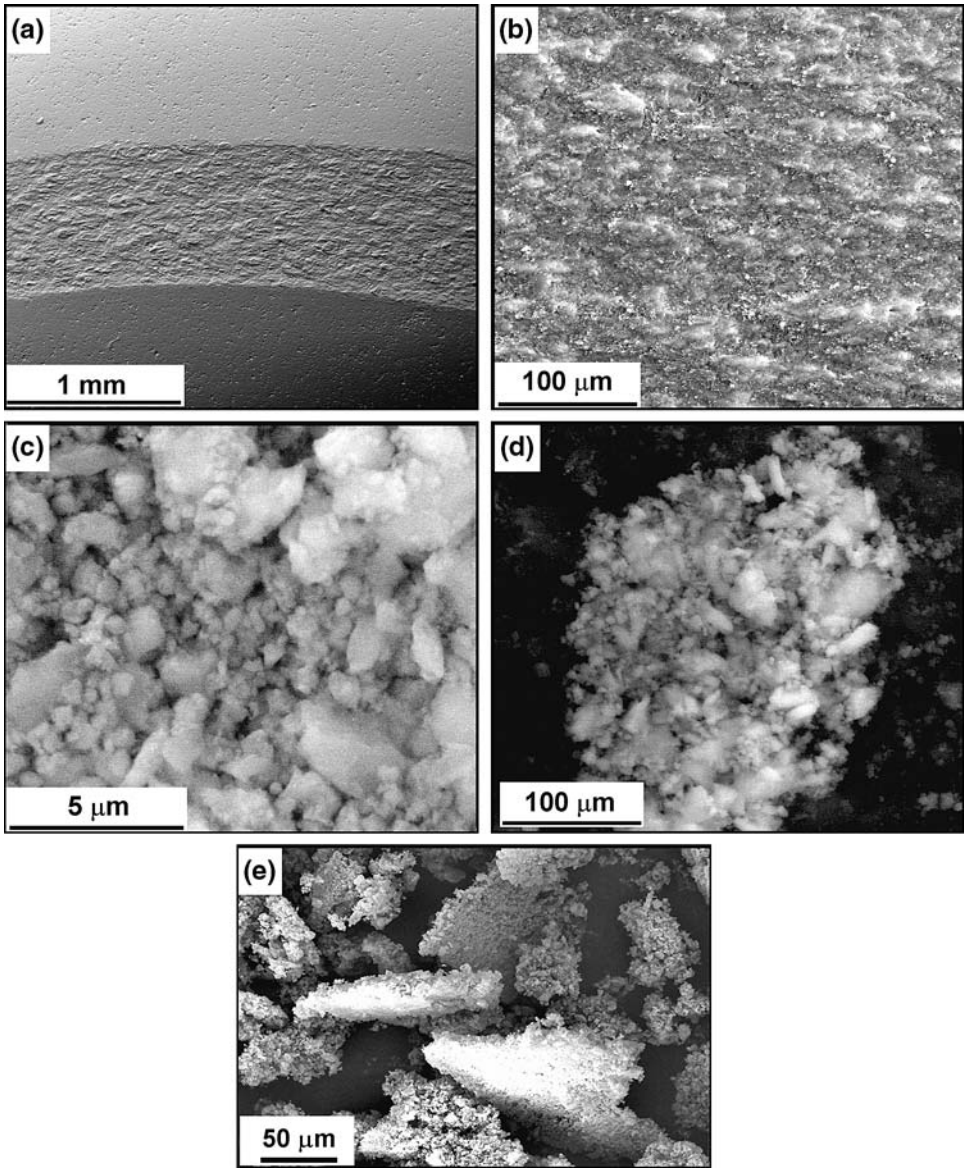

Fig. 12 Morphologies of the wear track and of the debris particles produced by ball-on-disk testing on APS Al_2O_3 coatings (room temperature): (a) wear track; (b) wear track, higher magnification; (c) wear track, detail showing small agglomerated particles; (d) agglomerated loose debris particle, detail; and (e) agglomerated debris particles with lamellar shape

Wear damage was restrained to some flattening of surface asperities. On the levelled asperities, a tribofilm is noticeable: this time, the tribofilm seems highly adherent and protective (Fig. 13b).

Probably, surface asperities are worn flat during the initial running in, and the tribofilm starts growing, until the contact area between the coating and the counterpart is large enough to reduce the contact pressure down to a value which does not cause any more wear on the coating. Indeed, in some roughness valleys inside the wear track (Fig. 13b, area indicated by circle), the original, unaltered coating surface appears: the small lamellae, formerly shown in Fig. 5, are very clearly recognizable in these regions, as shown in detail in Fig. 13(c).

Two factors are probably contributing to the suppression of further wear, once the initial tribofilm is formed. On the one hand, the HVSFS coating possesses stronger cohesion than conventional ones, as noted above; therefore, contact pressure reduction due to levelling of the initial asperities is sufficient to prevent extensive brittle fracture. In conventional coatings, by contrast, the contact pressure always remains high enough to produce brittle fracture. Indeed, in conventional thermally sprayed alumina-base coatings, cracks can propagate along interlamellar and intralamellar defects, leading to the removal of lamellae or of parts of them: this is generally recognized as their major source of wear loss (Ref 25-27).

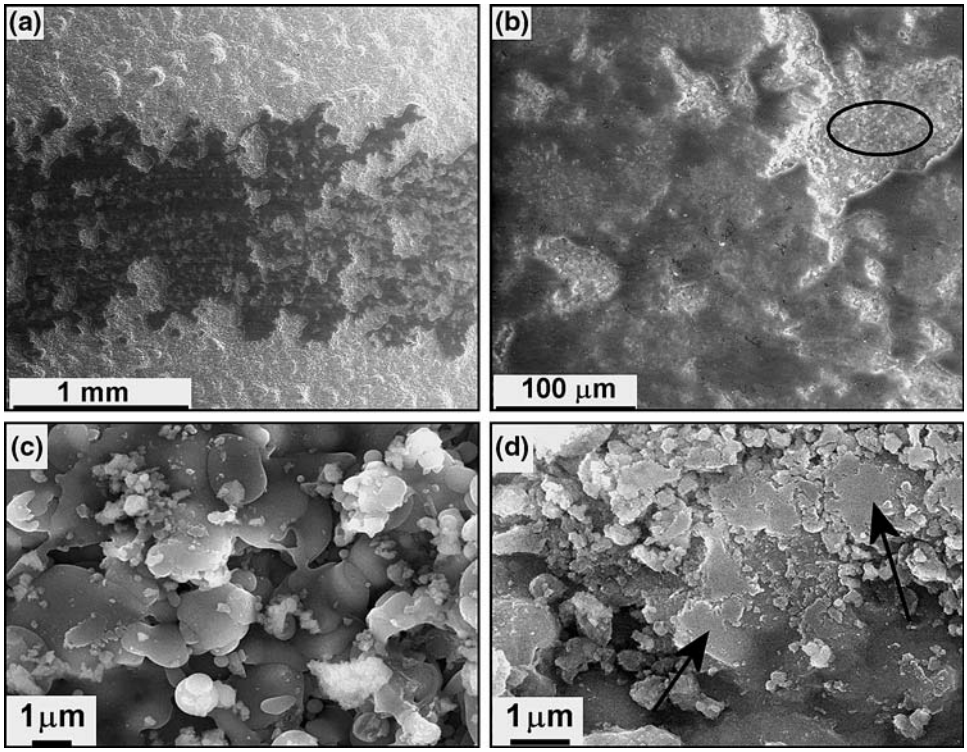

Fig. 13 Morphology of the wear track produced by ball-on-disk testing on HVSFS Al_2O_3 coatings (room temperature): (a) general view; (b) higher magnification; (c) detail of an unworn area, indicated by the circle in panel b; and (d) incipient plastic deformation of lamellae (see arrows)

On the other hand, the mechanisms leading to the formation of the tribofilm appear different in conventional coatings and HVSFS ones: whereas tribofilms on conventional coatings mainly consist of agglomerated debris particles, in HVSFS coatings the formation of the tribofilm seems largely due to microscale plastic deformation of the coating material (Fig. 13d). Microscale plastic deformation of lamellae is indeed recognizable on the worn surface of the HVSFS coating. A tribofilm formed by plastic deformation of the coating material obviously possesses higher cohesion and better protectiveness than the one formed by agglomerated debris particles. It is known that ceramic materials can undergo microscale plastic deformation (Ref 46, 47); however, up to now, such microscale plastic deformation of lamellae has mostly been described for thermally sprayed Cr_2O_3 (Ref 27, 48-50), which is known for its excellent tribofilm forming ability, rather than for Al_2O_3. As plastic deformation of ceramic materials mainly occurs by sliding along ''shear faults'' like grain boundaries (Ref 46, 47) or (in the case of thermally sprayed materials) lamellae boundaries (Ref 51), the much smaller lamella size and smaller intralamellar grain size of the HVSFS coating (as noted above) can promote better plastic deformation ability. The peculiar microstructure conferred by HVSFS spraying has therefore provided the Al_2O_3 coating with unique plastic deformation ability, enabling it to perform similarly to thermally sprayed Cr_2O_3, a coating material well-known for its excellent tribological qualities (Ref 52-54) but currently restrained, in some instances, by environmental regulations (Ref 55).

Accordingly, the tribofilm on the polished HVSFS Al_2O_3 coating also consists of a layer of plastically deformed material. Since the surface asperities of the as-deposited coating were removed by the polishing operation, the tribofilm extends to the whole wear track (Fig. 14a). Repeated local microscale plastic deformation eventually results in some fatigue cracking of the tribofilm (Fig. 14a), leading to limited tribofilm delamination phenomena, which are responsible for the small wear loss in this sample. Anyway, the difference between the depth of the wear groove on polished conventional Al_2O_3 and polished HVSFS Al_2O_3 is obvious (Fig. 14b, c), testifying the much better protectiveness of the tribofilm formed by the latter coating.

4. Conclusions

The microstructural features, micromechanical properties, and dry sliding tribological behavior of HVSFS Al_2O_3 coatings have been investigated and compared to those of conventional APS and HVOF-sprayed Al_2O_3 coatings. The HVSFS spraying technique allows near full melting of the particles fed via the suspension, resulting in

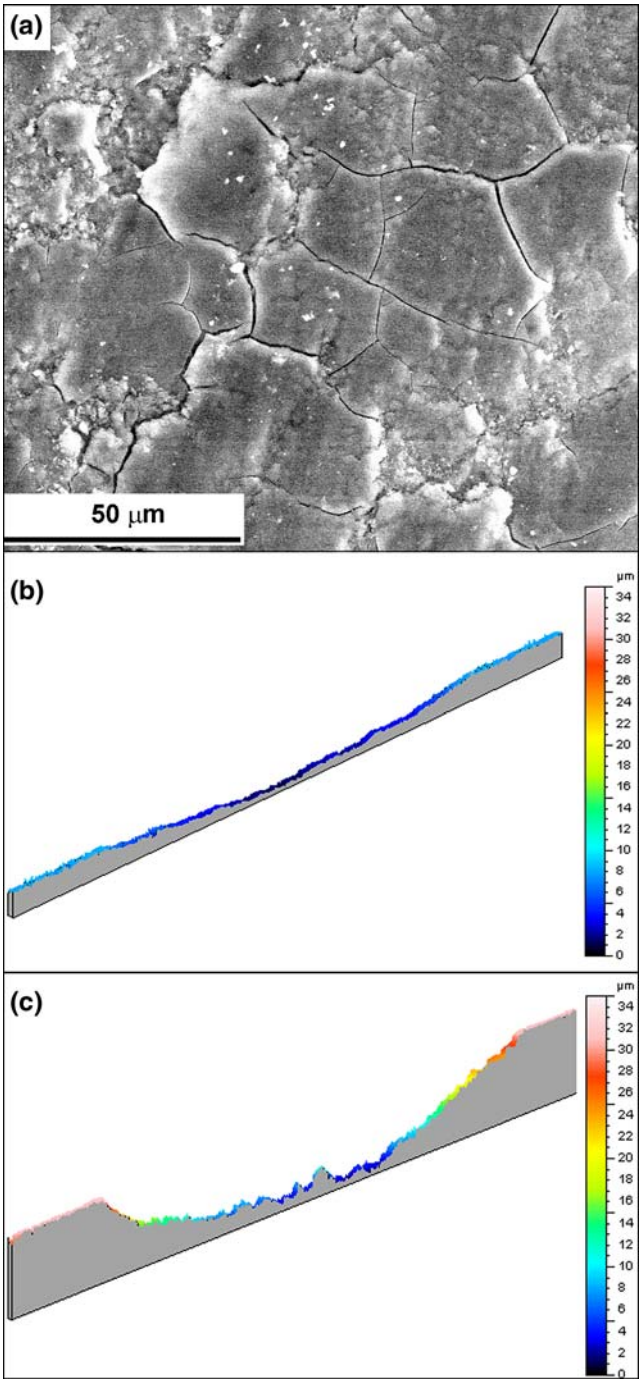

Fig. 14 Morphology of the wear track produced by ball-on-disk testing (room temperature) on polished HVSFS Al_2O_3 coating (a) and cross-sectional profiles of ball-on-disk wear grooves on polished HVSFS (b) and APS (c) coatings (vertical scales in panels b and c are the same)

very low amount of unmelted material in the coating (α-Al_2O_3/γ-Al_2O_3 ratio $<3\%$). The HVSFS-deposited coatings therefore possess lower porosity and smaller average pore size than conventional ones, so they are denser and exhibit higher protectiveness toward the substrate (high impedance values in EIS tests). Moreover, almost no interlamellar defects are found, and the very small lamellae do not develop transverse microcracking, unlike conventional thermal spray coatings: consequently, the amount of interconnected porosity is remarkably smaller than for APS and HVOF coatings. The favorable microstructural features of HVSFS coatings also reflect high inherent cohesion; indeed, increasing the Berkovich nanoindentation load does not cause as extensive cracking as for APS and HVOF conventional coatings. So, the dry sliding wear resistance of the HVSFS coating is definitely superior to that of conventional ones. Indeed, the small lamellae and the small intralamellar crystal size allow microscale plastic deformability, thus forming much more stable and protective tribofilms than on conventional coatings.

Acknowledgments

This work was partially supported by PRRIITT (Regione Emilia Romagna), Net-Lab ''Surface and Coatings for Advanced Mechanics and Nanomechanics'' (SUP&RMAN), and by MIUR (Funds ''Programmi per l'incentivazione del processo di internazionalizzazione del sistema universitario''). We are grateful to Dr. Antonio Candel for APS coating manufacturing. Thanks to Dr. Roberto Giovanardi for the assistance during EIS measurements and to Dr. Massimiliano Barletta for some of the profilometer measurements.

References

1. L. Xie, X. Ma, E.H. Jordan, N.P. Padture, D.T. Xiao, and M. Gell, Deposition of Thermal Barrier Coatings Using the Solution Precursor Plasma Spray Process, *J. Mater. Sci.*, 2004, **39**, p 1639-1646
2. E.H. Jordan, L. Xie, X. Ma, M. Gell, N.P. Padture, B. Cetegen, A. Ozturk, J. Roth, T.D. Xiao, and P.E.C. Bryant, Superior Thermal Barrier Coatings Using Solution Precursor Plasma Spray, *J. Therm. Spray Technol.*, 2004, **13**, p 57-65
3. L. Xie, X. Ma, A. Ozturk, E.H. Jordan, N.P. Padture, B.M. Cetegen, D.T. Xiao, and M. Gell, Processing Parameter Effects on Solution Precursor Plasma Spray Process Spray Patterns, *Surf. Coat. Technol.*, 2004, **183**, p 51-61
4. R. Rampon, F.-L. Toma, G. Bertrand, and C. Coddet, Liquid Plasma Sprayed Coatings of Yttria-Stabilized Zirconia for SOFC Electrolytes, *J. Therm. Spray Technol.*, 2006, **15**, p 682-688
5. C. Monterrubio-Badillo, H. Ageorges, T. Chartier, J.F. Coudert, and P. Fauchais, Preparation of $LaMnO_3$ Perovskite Thin Films by Suspension Plasma Spraying for SOFC Cathodes, *Surf. Coat. Technol.*, 2006, **200**, p 3743-3756
6. F.-L. Toma, G. Bertrand, D. Klein, C. Coddet, and C. Meunier, Nanostructured Photocatalytic Titania Coatings Formed by Suspension Plasma Spraying, *J. Therm. Spray Technol.*, 2006, **15**, p 587-592
7. F.-L. Toma, G. Bertrand, S. Begin, C. Meunier, O. Barres, D. Klein, and C. Coddet, Microstructure and Environmental Functionalities of TiO_2-Supported Photocatalysts Obtained by Suspension Plasma Spraying, *Appl. Catal. B*, 2006, **68**, p 74-84
8. A. Killinger, M. Kuhn, and R. Gadow, High-Velocity Suspension Flame Spraying (HVSFS), a New Approach for Spraying Nanoparticles with Hypersonic Speed, *Surf. Coat. Technol.*, 2006, **201**, p 1922-1929
9. X.Q. Ma, J. Roth, D.W. Gandy, and G.J. Frederick, A New High-Velocity Oxygen Fuel Process for Making Finely Structured and

Highly Bonded Inconel Alloy Layers from Liquid Feedstock, *J. Therm. Spray Technol.*, 2006, **15**, p 670-675
10. H. Kassner, R. Siegert, D. Hathiramani, R. Vassen, and D. Stoever, Application of Suspension Plasma Spraying (SPS) for Manufacture of Ceramic Coatings, *J. Therm. Spray Technol.*, 2008, **17**, p 115-123
11. P. Fauchais, R. Etchart-Salas, V. Rat, J.F. Coudert, N. Caron, and K. Wittmann-Ténèze, Parameters Controlling Liquid Plasma Spraying: Solutions, Sols, or Suspensions, *J. Therm. Spray Technol.*, 2008, **17**, p 31-59
12. B.G. Ravi, A.S. Gandhi, X.Z. Guo, J. Margolies, and S. Sampath, Liquid Precursor Plasma Spraying of Functional Materials: A Case Study for Yttrium Aluminum Garnet (YAG), *J. Therm. Spray Technol.*, 2008, **17**, p 82-90
13. M. Gell, E.H. Jordan, M. Teicholz, B.M. Cetegen, and N. Padture, Thermal Barrier Coatings Made by the Solution Precursor Plasma Spray Process, *J. Therm. Spray Technol.*, 2008, **17**, p 124-135
14. A. Wank, B. Wielage, H. Pokhmurska, E. Friesen, and G. Reisel, Comparison of Hardmetal and Hard Chromium Coatings Under Different Tribological Conditions, *Surf. Coat. Technol.*, 2006, **201**, p 1975-1980
15. P. Fauchais, Understanding Plasma Spraying, *J. Phys. D: Appl. Phys.*, 2004, **37**, p R86-R108
16. R. Gadow, A. Killinger, and J. Rauch, New Results in High Velocity Suspension Flame Spraying (HVSFS), *Surf. Coat. Technol.*, 2008, **202**(18), p 4329-4336
17. J. Stokes, The Theory and Application of the HVOF Thermal Spray Process, available on-line at http://webpages.dcu.ie/~stokesjt/ThermalSpraying/Book/HVOFThermalSpraying.htm, p 54-66
18. J.R. Davis, *Surface Engineering for Corrosion and Wear Resistance*, ASM International, Materials Park, OH, 2002, p 192-193
19. G. Bolelli, J. Rauch, V. Cannillo, A. Killinger, L. Lusvarghi, and R. Gadow, Preliminary Investigation of HVSFS Deposited Glass Coatings, *Mater. Lett.*, 2008, **62**, p 2772-2775
20. J.R. Davis, *Handbook of Thermal Spray Technology*, ASM International, Materials Park, OH, 2004, p 175-213
21. A. Kulkarni, S. Sampath, A. Goland, H. Herman, and B. Dowd, Computed Microtomography Studies to Characterize Microstructure-Property Correlations in Thermal Sprayed Alumina Deposits, *Scr. Mater.*, 2000, **43**, p 471-476
22. G. Antou, G. Montavon, F. Hlawka, A. Cornet, and C. Coddet, Characterizations of the Pore-Crack Network Architecture of Thermal-Sprayed Coatings, *Mater. Charact.*, 2004, **53**, p 361-372
23. F.-I. Trifa, G. Montavon, C. Coddet, P. Nardin, and M. Abrudeanu, Geometrical Features of Plasma-Sprayed Deposits and Their Characterization Methods, *Mater. Charact.*, 2005, **54**, p 157-175
24. C.-J. Li and A. Ohmori, Relationships Between the Microstructure and Properties of Thermally Sprayed Deposits, *J. Therm. Spray Technol.*, 2002, **11**, p 365-374
25. R. Westergård, L.C. Erickson, N. Axén, H.M. Hawthorne, and S. Hogmark, The Erosion and Abrasion Characteristics of Alumina Coatings Plasma Sprayed Under Different Spraying Conditions, *Tribol. Int.*, 1998, **31**, p 271-279
26. H.M. Hawthorne, L.C. Erickson, D. Ross, H. Tai, and T. Troczynski, The Microstructural Dependence of Wear and Indentation Behaviour of Some Plasma-Sprayed Alumina Coatings, *Wear*, 1997, **203-204**, p 709-714
27. G. Bolelli, V. Cannillo, L. Lusvarghi, and T. Manfredini, Wear Behaviour of Thermally Sprayed Ceramic Oxide Coatings, *Wear*, 2006, **261**, p 1298-1315
28. G. Bolelli, L. Lusvarghi, T. Manfredini, F. Pighetti Mantini, R. Polini, E. Turunen, T. Varis, and S.-P. Hannula, Comparison Between Plasma- and HVOF Sprayed Ceramic Coatings. Part I: Microstructure and Mechanical Properties, *Int. J. Surf. Sci. Eng.*, 2007, **1**, p 38-61
29. H. Du, J.H. Shin, and S.W. Lee, Study on Porosity of Plasma Sprayed Coatings by Digital Image Analysis Method, *J. Therm. Spray Technol.*, 2005, **14**, p 453-461
30. G. Antou, G. Montavon, F. Hlawka, A. Cornet, and C. Coddet, Exploring Thermal Spray Gray Alumina Coating Pore Network Architecture by Combining Stereological Protocols and Impedance Electrochemical Spectroscopy, *J. Therm. Spray Technol.*, 2006, **15**, p 765-772
31. J. Zhang and V. Desai, Evaluation of Thickness, Porosity and Pore Shape of Plasma Sprayed TBC by Electrochemical Impedance Spectroscopy, *Surf. Coat. Technol.*, 2005, **190**, p 98-109
32. W.C. Oliver and G.M. Pharr, An Improved Technique for Determining Hardness and Elastic Modulus Using Load and Displacement Sensing Indentation Experiments, *J. Mater. Res.*, 1992, **7**, p 1564-1583
33. L. Bianchi, A. Denoirjean, F. Blein, and P. Fauchais, Microstructural Investigation of Plasma-Sprayed Ceramic Splats, *Thin Solid Films*, 1997, **299**, p 125-135
34. R.J. Damani and A. Wanner, Microstructure and Elastic Properties of Plasma-Sprayed Alumina, *J. Mater. Sci.*, 2000, **35**, p 4307-4318
35. A. Kulkarni, J. Gutleber, S. Sampath, A. Goland, W.B. Lindquist, H. Herman, A.J. Allen, and B. Dowd, Studies of the Microstructure and Properties of Dense Ceramic Coatings Produced by High-Velocity Oxygen-Fuel Combustion Spraying, *Mater. Sci. Eng. A*, 2004, **369**, p 124-137
36. L. Li, B. Kharas, H. Zhang, and S. Sampath, Suppression of Crystallization During High Velocity Impact Quenching of Alumina Droplets: Observations and Characterization, *Mater. Sci. Eng. A*, 2007, **456**, p 35-42
37. S. Basu and B.M. Cetegen, Modeling of Liquid Ceramic Precursor Droplets in a High Velocity Oxy-Fuel Flame Jet, *Acta Mater.*, 2008, **56**(12), p 2750-2759
38. S. Basu, E.H. Jordan, and B.M. Cetegen, Fluid Mechanics and Heat Transfer of Liquid Precursor Droplets Injected into High-Temperature Plasmas, *J. Therm. Spray Technol.*, 2008, **17**, p 60-72
39. J. Fazilleau, C. Delbos, V. Rat, J.F. Coudert, P. Fauchais, and B. Pateyron, Phenomena Involved in Suspensions Plasma Spraying. Part 1: Suspensions Injection and Behaviour, *Plasma Chem. Plasma Process.*, 2006, **26**, p 371-391
40. J. Fazilleau, C. Delbos, V. Rat, J.F. Coudert, P. Fauchais, and B. Pateyron, Phenomena Involved in Suspensions Plasma Spraying. Part 2: Zirconia Particle Treatment and Coating Formation, *Plasma Chem. Plasma Process.*, 2006, **26**, p 393-414
41. J. Oberste Berghaus, J.-G. Legoux, C. Moreau, F. Tarasi, and T. Chráska, Mechanical and Thermal Transport Properties of Suspension Thermal-Sprayed Alumina-Zirconia Composite Coatings, *J. Therm. Spray Technol.*, 2008, **17**, p 91-104
42. S. Ghosh, S. Das, T.K. Bandyopadhyay, P.P. Bandyopadhyay, and A.B. Chattopadhyay, Indentation Responses of Plasma Sprayed Ceramic Coatings, *J. Mater. Sci.*, 2003, **38**, p 1565-1572
43. L. Prchlik and S. Sampath, Effect of the Microstructure of Thermally Sprayed Coatings on Friction and Wear Response Under Lubricated and Dry Sliding Conditions, *Wear*, 2007, **262**, p 11-23
44. G. Bolelli, V. Cannillo, L. Lusvarghi, F. Pighetti Mantini, E. Gualtieri, and C. Menozzi, An FIB Study of Sharp Indentation Testing on Plasma-Sprayed TiO_2, *Mater. Lett.*, 2008, **62**, p 1557-1560
45. K. Duan and R.W. Steinbrech, Influence of Sample Deformation and Porosity on Mechanical Properties by Instrumented Microindentation Technique, *J. Eur. Ceram. Soc.*, 1998, **18**, p 87-93
46. K. Hokkirigawa, Wear Mode Map of Ceramics, *Wear*, 1991, **151**, p 219-228
47. K. Kato and K. Adachi, Wear of Advanced Ceramics, *Wear*, 2002, **253**, p 1097-1104
48. H.-S. Ahn and O.-K. Kwon, Tribological Behaviour of Plasma-Sprayed Chromium Oxide Coating, *Wear*, 1999, **225-229**, p 814-824
49. Y. Jin and Y. Yang, Tribological Behaviour of Various Plasma-Sprayed Ceramic Coatings, *Surf. Coat. Technol.*, 1996, **88**, p 248-254
50. G. Bolelli, L. Lusvarghi, T. Manfredini, F. Pighetti Mantini, E. Turunen, T. Varis, and S.-P. Hannula, Comparison Between Plasma- and HVOF-Sprayed Ceramic Coatings. Part II: Tribological Behaviour, *Int. J. Surf. Sci. Eng.*, 2007, **1**, p 62-79
51. Y. Xie and H.M. Hawthorne, The Damage Mechanisms of Several Plasma Sprayed Ceramic Coatings in Controlled Scratching, *Wear*, 1999, **233-235**, p 293-305

52. K.G. Budinsky, Abrasion Resistance of Transport Roll Surfaces, *Wear*, 1995, **181-183**, p 938-943
53. R.B. Heimann, Applications of Plasma-Sprayed Ceramic Coatings, *Key Eng. Mater.*, 1996, **122-124**, p 399-442
54. R. Winkler, F. Bültmann, S. Hartmann, and H. Burkard, 316L – An Alternative to NiCr Bondcoats for Cr_2O_3-Coatings on Anilox Rolls, *Thermal Spray 2003: Advancing the Science and Applying the Technology*, B.R. Marple and C. Moreau, Eds., May 5-8, 2003 (Orlando, FL), ASM International, 2003, p 149-152
55. State of California Air Resources Board, Resolution 04-44, December 9, 2004; available on-line at: http://www.arb.ca.gov/regact/thermspr/res0444.pdf